

Research Article

Strain Monitoring of Combustible Gas Implosion Test Based on Fiber Bragg Grating

Lei Gao,^{1,2} Qinghua Zhang^{1,2}, Erbing Li,² Yangyang Sun^{1,2}, Zhenglin Zhang,² Shikun Pu,² Xiejun Cheng,³ and Fengjuan Rong²

¹College of Mechanical Engineering, Nanjing University of Science and Technology, Nanjing 210094, China

²Army Engineering University of PLA, Nanjing 210007, China

³Jiangsu Second Normal University, Nanjing 210013, China

Correspondence should be addressed to Qinghua Zhang; 1522475731@qq.com

Received 23 January 2019; Revised 27 April 2019; Accepted 5 May 2019; Published 28 May 2019

Academic Editor: Georges Kouroussis

Copyright © 2019 Lei Gao et al. This is an open access article distributed under the Creative Commons Attribution License, which permits unrestricted use, distribution, and reproduction in any medium, provided the original work is properly cited.

Strain measurement is an important component in model tests of combustible internal explosions. Strain gauges are used to measure strain in traditional electrical measurement methods and have some limitations, such as susceptibility to electromagnetic interference, short life, and inability to distribute. Fiber Bragg gratings (FBGs) are developing into useful sensing tools that can respond to changes in stress, strain, and temperature by changing wavelengths. FBGs have excellent sensing performance, such as long life, antielectromagnetic interference, easy networking, and good reusability. In this paper, FBG sensors are applied to strain monitoring in ethylene flammable implosion experiments. In the ethylene flammable implosion tests, an FBG was placed on the inner surface of the bottom plate of the rectangular steel test device near the detonation vent by the sticking method. The reliability and repeatability of the strain change of the FBG affected by detonation overpressure and combustion were tested at this point. Four explosion tests were carried out. The test results showed that FBG sensors could obtain stable and reliable strain data in all four tests. The strain variation reflects the development of overpressure and combustion in the whole process from ignition. For the strain amplitude formed by overpressure, the minimum was $1.449 \mu\epsilon$ (the third test), and the maximum was $48.181 \mu\epsilon$ (the fourth test). For the strain amplitude step change formed by the deflagration flame front passing the measurement points, the minimum was $1.673 \mu\epsilon$ (the second test), and the maximum was $19.724 \mu\epsilon$ (the fourth test). The strain amplitude produced by the deflagration temperature effect in the four tests ranged from $72.803 \mu\epsilon$ (the first test) to $143.381 \mu\epsilon$ (the fourth test). The results show that FBG sensors can provide reliable and effective strain monitoring data for the experimental study of flammable implosions.

1. Introduction

The rapid development of industrial production has led to frequent explosions and fire disasters [1]. To serve the explosion-proof and explosion venting designs of industrial buildings, we need to conduct targeted studies on the destructive effects of flammable gas implosion. Since combustible gas implosion involves many theories, such as thermodynamics, fluid mechanics, chemical kinetics, heat transfer medium, and turbulent medium, the mechanism is very complicated and difficult to describe accurately [2–4]. A common and effective method is to study the combustion

and explosion processes of combustible gases through model tests. To analyze the pressure and flame velocity propagation rules during a deflagration process, an effective test method is to test the stress and strain changes inside the test device.

At present, electrical measuring methods are widely used in strain measurement. The resistance strain gauges commonly used in electrical measuring methods have the advantages of small volume, high sensitivity, high-frequency response, etc., and are widely used in stress and strain measurements of dams, bridges, space shuttles, ship structures, power generation structures, etc. [5–7]. In the static structure test of the Boeing 767 aircraft in the United States,

more than 2000 strain gauges and more than 1000 strain rosettes were used to measure the strain data of a large number of parts of the aircraft structures [6]. However, there are also some problems that cannot be ignored: (1) because of the existence of zero drift, the measurement process is not conducive to cumulative monitoring; (2) measurements are vulnerable to electromagnetic interference and external environmental impacts; (3) it is not easy to form a sensor network; and (4) the service life of a strain gauge is short.

Fiber Bragg gratings (FBGs) are excellent sensors with advantages of long service life, antielectromagnetic interference, good reusability, and capability to connect in series and are widely used in deformation monitoring of large equipment. Davis et al. [8] used a wavelength division multiplexing FBG sensing network to perform morphometrics on a cantilever beam structure and used the Rayleigh–Ritz rule to optimize the strain data obtained by fiber grating sensing to accurately predict shapes of the simple cantilever beam. Arritt et al. [9] used an integrated FBG sensor to perform morphological sensing and reconstruction of large expandable spatial structures, demonstrating the application potential of fiber sensing technology in the morphological monitoring of large-scale spatial structures. Ya et al. [10] in professor Qian Jinwu's research group studied a method of measuring the spatial curvature information of a structure by using an FBG sensor array to reconstruct the structural morphology, including the line shape and the rod shape; this method was mainly used for bending and positioning of underground pipelines, real-time detection of robots' endoscopic shapes, dynamic detection of solar panel surface shapes, and spatial shape reconstruction of ruin search-and-rescue robots.

In the field of aerospace, Wolfgang E et al. used 12 FBG sensors to construct a distributed strain and temperature sensing network to monitor the hull structure of the reentry vehicle X-38 [11]. In 2003, since the "Sun God" UAV had disintegrated in air due to excessive wing deformation, the Dryden Flight Research Center proposed a new real-time strain monitoring technology based on FBG sensors [12, 13]. Boeing's Variable Geometry Chevrons (VGCs) research program used a high-density distributed FBG shape sensing system developed by L to monitor the morphological characteristics of the V-shaped structure at the trailing edge of an engine's jet nozzle under different flight conditions.

FBGs have been applied in safety monitoring studies of engineering structures, have achieved many results, and have mainly been used to measure an object's strain, pressure, displacement, vibration, cracks and other information. Ou et al. [14] and Chan et al. [15] used FBG sensors for structural health monitoring of bridges, including 40 grating sensors for strain monitoring at different parts, and obtained good monitoring results. Zhu et al. [16] developed monitoring instruments such as FBG strain gauges, thermometers, settlement gauges, and horizontal inclinometers to monitor the strain, temperature, and displacement of the ground and foundations in ground foundation health monitoring. Sun [17] pasted an FBG to a submarine pipeline model for vibration testing to test that

the FBG strain sensor had good working performance for low-frequency vibration system monitoring in a study of the dynamic characteristics and application ranges of FBG strain sensors. Zhang et al. [18, 19] applied FBG sensors to test concrete structure cracks and gravel soil landslides and verified the application of FBGs in the safety monitoring of civil engineering structures.

With the development of demodulation technology, the application of FBGs in high-frequency vibration environments has begun and developed [20, 21]. Wu et al. [22] simulated rock impact in the interior of the Earth in the laboratory, used FBGs to detect the shock signal generated, and compared the results with those measured by a seismic geophone. The experimental results showed that when the vibration signal was in the range of 100–2500 Hz, the results obtained by the detection system were in good agreement with the actual situation. A. Cusano et al. [23] studied a method that can simultaneously measure dynamic and static strains. The detection principle is that a broadband light source enters the sensing grating through a coupler, and the light reflected by the fiber grating enters an asymmetric optical filter. The transmitted and reflected light signals of the filter are detected by a photoelectric detector, and then, the sensing signals are demodulated by a circuit operation. Zhu et al. [24] tested the high-frequency vibration signal of a deformed split Hopkinson pressure bar test device, and the FBG high-frequency strain test system had a good response to a signal with a frequency of less than 8 kHz.

Rodriguez et al. [25] explored two types of FBG sensing systems that aim to apply this technology as embedded high-pressure probes for transient shock events, and the sensing systems are used to "monitor the spectral shifts of FBGs that are immersed into liquid water and shock compressed using explosives." Karabacak et al. [26] developed a high-speed system for FBG-based measurements of vibration and sound in a wide range of applications from seismic surveys to machine and structural monitoring applications in harsh environments. Sun et al. [27] used FBGs to monitor the surface strain of concrete structures under explosive impact and verified the applicability of FBGs to structural strain monitoring under high frequency and strong impact. Rodriguez [28] presented a demonstration of both chirped and uniform silica-based FBGs for sensing under harsh conditions that varied from thermal ignition in high explosives to inert tracking of high-pressure shock waves, and the demonstration used coherent broadband pulses from a femtosecond mode-locked fiber laser at 1560 nm to illuminate and interrogate the FBGs at a repetition rate of 100 MHz. However, few studies have applied FBGs in gas implosion testing.

In this paper, the FBG sensor is used to test the strain monitoring performance of explosion cave's inner surface during the deflagration process in the ethylene combustible gas implosion test, which is pasted to the inner surface of the explosion cave. The FBG is proved to be capable of accurately monitoring the strain change of the inner surface of the structure caused by overpressure after deflagration of combustible gas in high-temperature and high-pressure environments.

2. FBG Sensor and Dynamic Strain Measurement Analysis

2.1. FBG Sensing Principle. An FBG utilizes the photosensitivity of fiber materials to form a spatial phase grating in the fiber core, and this process essentially forms a narrow-band (transmissive or reflective) filter or reflector in the fiber core, as shown in Figures 1(a) and 1(b); the optical properties of this filter or reflector are controlled by the physical quantities of the external environment, thereby constituting an FBG sensor. The reflection spectrum of a Bragg grating is mainly determined by its bandwidth and peak reflectivity, which in turn are functions of parameters such as the grating length and refractive index modulation factor.

Any physical process in which these parameters (such as temperature and stress) are changed will cause the grating Bragg wavelength to drift, as shown in Figure 2. Establishing and calibrating the relationship between the change in the center wavelength of the FBG and the measured value can be obtained by the change in the center wavelength of the FBGs. The reflection condition is

$$\lambda_B = 2n_{\text{eff}} \cdot \Lambda, \quad (1)$$

where λ_B is the center wavelength of the grating, n_{eff} is the effective refractive index, and Λ is the grating pitch.

The relationship between the amount of change in the central wavelength and strain and temperature is shown in the following formula:

$$\frac{\Delta\lambda_B}{\lambda_B} = (1 - P)\varepsilon + (\alpha + \xi)\Delta T. \quad (2)$$

If $K_\varepsilon = \lambda_B(1 - P)$, $K_T = \lambda_B(\alpha + \xi)$, and formula (2) is changed to

$$\Delta\lambda_B = K_\varepsilon\varepsilon + K_T\Delta T. \quad (3)$$

In formula (3), K_ε is the FBG strain sensing sensitivity coefficient, and K_T is the FBG temperature sensing sensitivity coefficient. For general quartz fiber, $P = 0.22$, $\alpha = 0.55 \times 10^{-6}/^\circ\text{C}$, and $\xi = 6.67 \times 10^{-6}/^\circ\text{C}$. When $\lambda_B = 1550 \text{ nm}$, $K_\varepsilon = 1.2 \text{ pm}/\mu\varepsilon$ and $K_T = 11.19 \text{ pm}/^\circ\text{C}$.

2.2. Analysis of Dynamic Response Characteristics of FBG Sensors. In a combustible gas implosion test, gas combustion is a rapidly developing process. To capture the effect of the detonation vent on deflagration overpressure, this paper presents the application of an FBG in the strain monitoring of the inner surface of an ethylene flammable implosion test device to test the strain monitoring performance of FBGs in the processes of deflagration, detonation, and discharge. The FBG is used to monitor the internal deflagration strain of the combustible gas, and the focus is on analysis of the frequency response, range, strain transfer ratio, and packaging protection.

- (1) Frequency response: according to the literature [29], the combustible gas deflagration pressure rise becomes slower, generally lasting for 100~300 ms. Therefore, when the sensor's data sampling interval

is set at least on the order of milliseconds, a sufficient amount of data can be collected. The grating sensor demodulator used in this experiment is the MOI-SM130 series manufactured by MOI Corporation of the United States, and its sampling frequency is 2 kHz, which can meet the frequency response requirements of the strain generated by the combustible gas implosion impact.

- (2) Range: the test device is made of 304 stainless steel with a thickness of 10 mm and can withstand a maximum overpressure of approximately 0.5 MPa; the equivalent static load is generally 2 times overpressure for 1 MPa [29]. Regardless of the impact effect, according to the material constitutive model, the strain of steel under 1 MPa is approximately 5 microstrains, and the maximum strain limit allowed for the bare FBG is approximately 3000 [27, 30, 31]. Therefore, the grating sensor can fully meet the range requirements for measuring the strain on the inner surface of the test device.
- (3) Strain transfer: the grating sensor must be packaged and pasted to obtain the strain of the steel plate, and the paste used is generally instant adhesive or epoxy resin. Since the adhesive layer has a certain thickness, it is necessary to consider the influences of the adhesive layer on the strain response and strain transfer when acquiring high-frequency measurements. According to the literature [27, 31, 32], the bare FBG is used to measure the strain of the equal-strength beam and concrete specimen by adhesive paste (502 instant adhesive, epoxy resin). When the FBG length is approximately 1.5 cm, the pasting length is more than 3 cm and the thickness of the adhesive layer is less than 100 microns, so the strain transfer ratio can reach 96% under static force loading. According to the above analysis, the bare grating fiber is directly pasted on the inner surface of the test device by the instant adhesive (the test device is a ferroalloy), and the pasting length is ensured to be more than 3 cm (the FBG length is approximately 1.5 cm).
- (4) Packaging protection: the unpackaged FBG directly acts as a strain sensor, and its operating temperature is -20~75 degrees, but the combustible gas explosion process will generate a large heat release. For example, methane and ethylene air-mixed gas will instantaneously have a high temperature; if the grating device is directly exposed at this high temperature, it will fail or be damaged even if the time is short, and the acquired data will also be influenced by the temperature. Therefore, in the combustible gas implosion test, thermal insulation protection measures need to be adopted for the grating optical cable.

According to the above analysis, the grating strain measurement test of the ethylene combustible gas implosion test device is designed in this paper. According to the

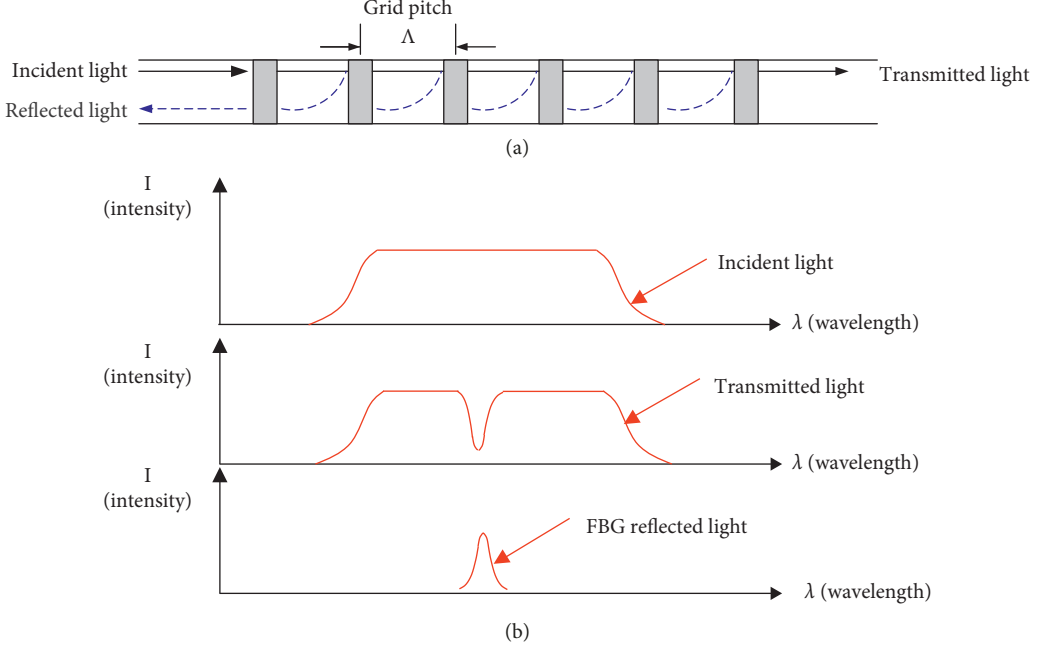


FIGURE 1: Schematic diagram of grating reflection.

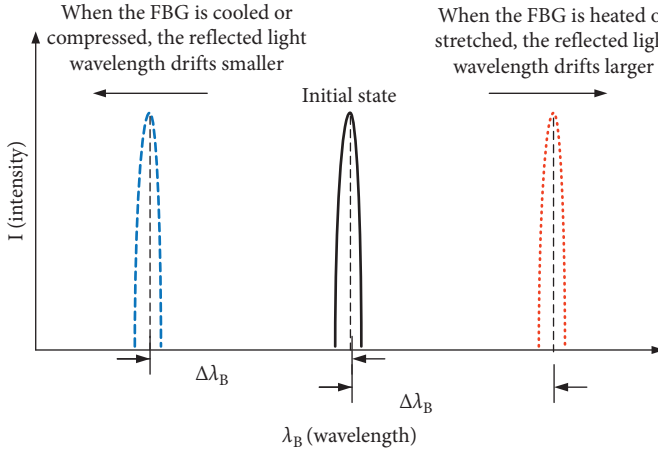


FIGURE 2: Schematic diagram of temperature and strain corresponding to wavelength changes.

characteristics of the grating sensor, the grating sensor is packaged and pasted on the bottom inner surface of the test device by adopting a reasonable and effective paste protection method to obtain the changes in the internal surface strain of the device formed by the overpressure shock and the wavelength of the high temperature formed by the flame front passing by the grating sensor.

3. Experimental Design

3.1. Combustible Gas Implosion Testing Device. In the experiment, the test device has a square main body and is 2 m long, with an internal section size of $1.1 \text{ m} \times 0.5 \text{ m}$, a wall thickness of 10 mm, and an internal volume of 1.1 m^3 . The device is made of 304 stainless steel and can endure a

maximum overpressure of 0.5 MPa. One end is opened with a 70 mm round hole, welded flange, high-strength bolt, sealing gasket, etc., and can be connected to a circular shock tube; the other end is in the form of a hinged buckle cover and is easy to open and close, as shown in Figure 3. The top is opened with a digital display vacuum meter mounting hole with a size of M20 × 1.5; the container side has six M20 × 1.5 holes along the axis for installing the inlet pipe; and the bottom is provided with two fixed brackets.

In this test, the combination of a 24 V DC power supply and a resistance wire is used to heat the wire to ignite the gas mixture inside the container. By means of the fine resistance wire and gunpowder, the electric resistance wire is energized and heated to detonate the gunpowder wrapped around the



FIGURE 3: Rotary pressure relief member of the explosion container, ignition system, gas transmission system, and measurement system.

electric resistance wire. The ignition energy is approximately 100 J. Ignition was achieved by means of an end-mounted, electrically activated match having a stored energy of 100 J. The combustible gas for testing is ethylene gas; the inlet pipe is a bellows of $\Phi 32$ mm, and the two ends are connected by clamps and joints to ensure the sealing of the vacuum system.

The gas deflagration test device includes four parts: the explosion container, ignition system, gas transmission system, and measurement system, as shown in the schematic diagram in Figure 4. Pressure sensors (PCB113B24) are used to measure the explosion overpressure. A pressure gauge is used to measure the pressure inside the device to estimate the ethylene gas concentration.

3.2. Test Measurement and Data Acquisition System. The grating sensor used in the experiment is a bare grating, and the interrogator is an SM130FBG interrogator manufactured by MOI Corporation of the United States, as shown in Figure 5. The interrogator can identify FBG sensors with a center wavelength between 1510 nm and 1590 nm and wavelength resolution up to 1 pm, can realize 4-channel synchronous 2 kHz sampling, and can realize simultaneous measurement of 16 channels after being externally connected to an expansion module.

The implosion pressure of the container is measured by the pressure sensor on the upper side of the experimental device, as shown in Figure 4; a grating strain sensor is pasted to the lower surface of the device near the explosion vent. The strain gauges are placed on the pressure relief door window and the edges of the structure, and the breakage of the strain sensor indicates that the explosion vent is open, which is used to determine the initial moment when the explosion vent is opened. After the gas explosion, the pressure acts on the members and the sensors at the same time. The pressure sensor and the grating and the strain sensor output electrical signals of the reaction pressure and the strain, and these signals are collected and recorded by the test system. Additionally, a high-speed camera (the shooting interval is 1 ms) is in trigger association with the pressure sensor, and the pressure data corresponding to the time at which the strain gauge is broken correspond to the image at the initial moment in the high-speed photography; therefore, the opening process of the pressure relief member, the

internal pressure change, and the opening of the explosion vent can be obtained.

3.3. Grating Layout and Strain Transfer Analysis. The FBG sensor is pasted to the inner surface of the test device, as shown in Figure 6. Figure 7 shows a perspective view of the test device.

Figure 8 shows an electron microscopy image in which the coating layer free grating is pasted on a steel plate. The shiny part at the bottom is the steel plate substrate, the shiny circle in the middle is the grating, and the darker part between the grating and the substrate is the pasting glue.

The position required for pasting the grating on the bottom plate of the test device is smoothed with sand paper, and the grating sensor is fixed and evenly coated with 502 instant adhesive. After the adhesive is solidified, tape is applied on the surface of the sensor for protection, and the surface of the tape is coated with butter for insulation. The paste model is shown in Figure 9.

Due to the protection of the butter, tape, and 502 adhesive, the strain caused by the impact load directly acting on the grating sensor is very small and can be ignored. The strain of the grating refers to the grating coordinated deformation mainly caused by deformation of the steel plate where the grating is pasted due to the influences of the impact and temperature.

According to the literature [30], for both the tube package and the substrate package, the lag time of the strain wave transfer from the substrate to the FBG is on the order of 10^{-7} s, and the deflagration pressure rise time is on the order of 10^{-2} s, so the propagation times of the strain wave in the adhesive layer and the packaging layer can be negligible. In this test, the bare grating is directly pasted to the inner surface of the test device. Compared with the FBG sensors packaged by the tube and substrate, bare FBG directly pasted has less amplification effect on actual strain [33].

After the combustible gas is imploded, the implosion overpressure acts on the inner surface of the device, and the steel plate is deformed under pressure. The sectional view along the x direction is shown in Figure 10(b). The wavelength change of the grating sensor reflects the compressive strain of the steel plate at the point in the x direction under the impact

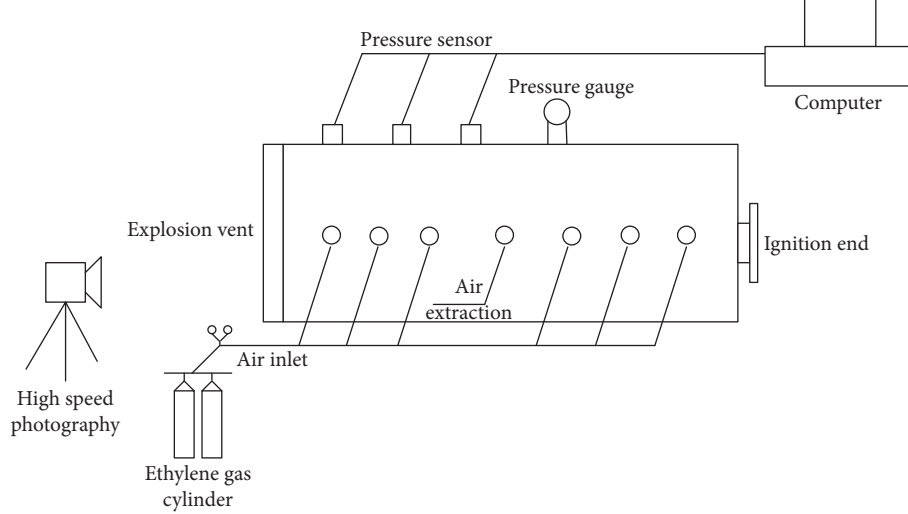


FIGURE 4: Schematic diagram of the test device.



FIGURE 5: Grating sensor data acquisition system.

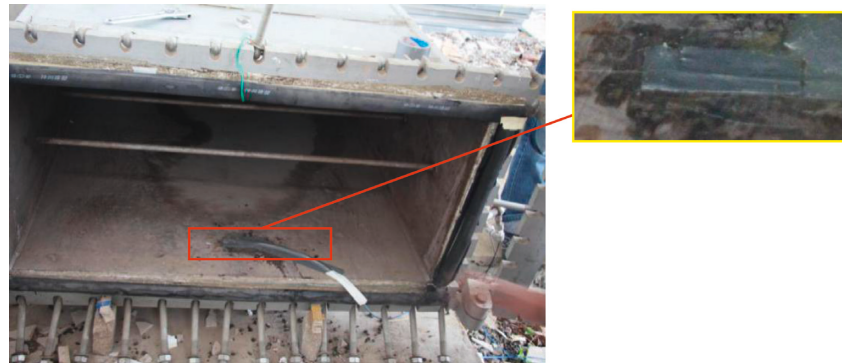


FIGURE 6: FBG sensor.

load. The steel plate expands with the gradually increasing temperature, and the wavelength change of the grating sensor reflects the tensile strain due to thermal expansion.

4. Test Data Analysis

Four deflagration tests were performed in this experiment. The volume ratio of ethylene was approximately 6~7%, and the explosion vent was pasted and closed with tape. The explosion vent of the test device is in the form of a hinged

buckle cover, and the opening rule is that the venting area is gradually increased. According to the literature [16–20], combustible gas implodes in an explosion cave with an open explosion vent, and a certain overpressure is reached in the explosion cave before the explosion vent is opened; after the explosion vent is opened, a second overpressure may occur according to the emission situation of the combustible gas. The inner surface of the test device is subjected to an impact that forms a strain that changes as the implosion overpressure changes.

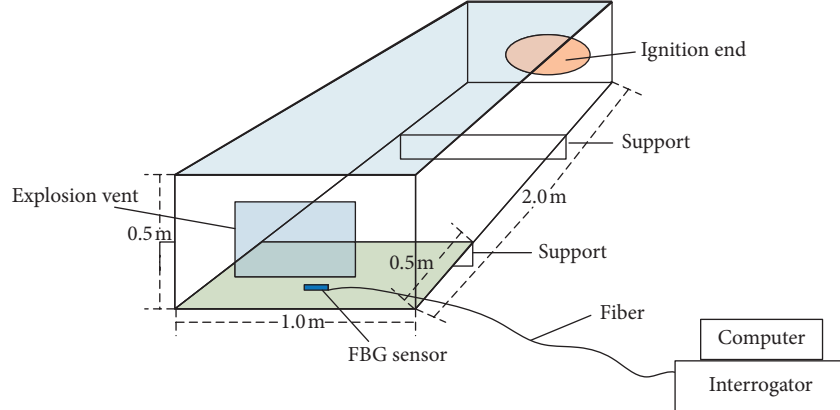


FIGURE 7: Test device dimensions and sensor position.

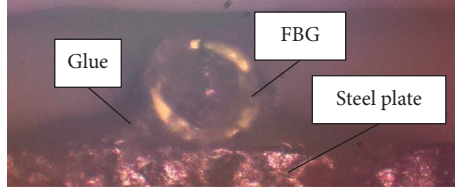


FIGURE 8: Electron microscopy image of the coating layer free FBG after pasting.

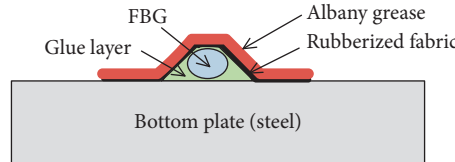
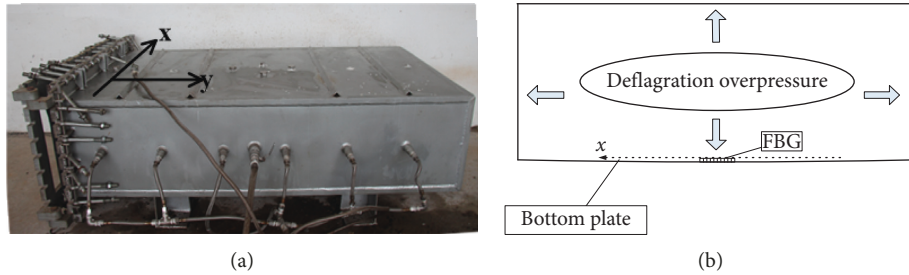


FIGURE 9: Schematic diagram of strain transfer for the bottom grating sensor of the test device.

FIGURE 10: Schematic diagram of the strain of the FBG measurement in the x direction. (a) Test device. (b) Cross-sectional view in the x direction.

4.1. First Test. In the first test, the volume ratio of ethylene was approximately 6%, and the strain change measured by the FBG sensor is shown in Figure 11.

Three windows are selected for analysis, marked as window 1-1, window 1-2, and window 1-3 in Figure 11. Figure 12 shows the enlarged window 1-1 results. There are two peaks in the strain change measured by the FBG. Combined with the working condition, the implosion

formed the initial overpressure after ignition while the explosion vent was not opened. Under the action of the initial overpressure, the first peak in the FBG strain appears, as shown in Figure 12, indicated by the peak 1 arrow. Furthermore, the initial overpressure leads to the opening of the explosion vent, and the combustible material is vented in full contact with the air; the deflagration intensifies, and the vented overpressure is formed. Under the action of the

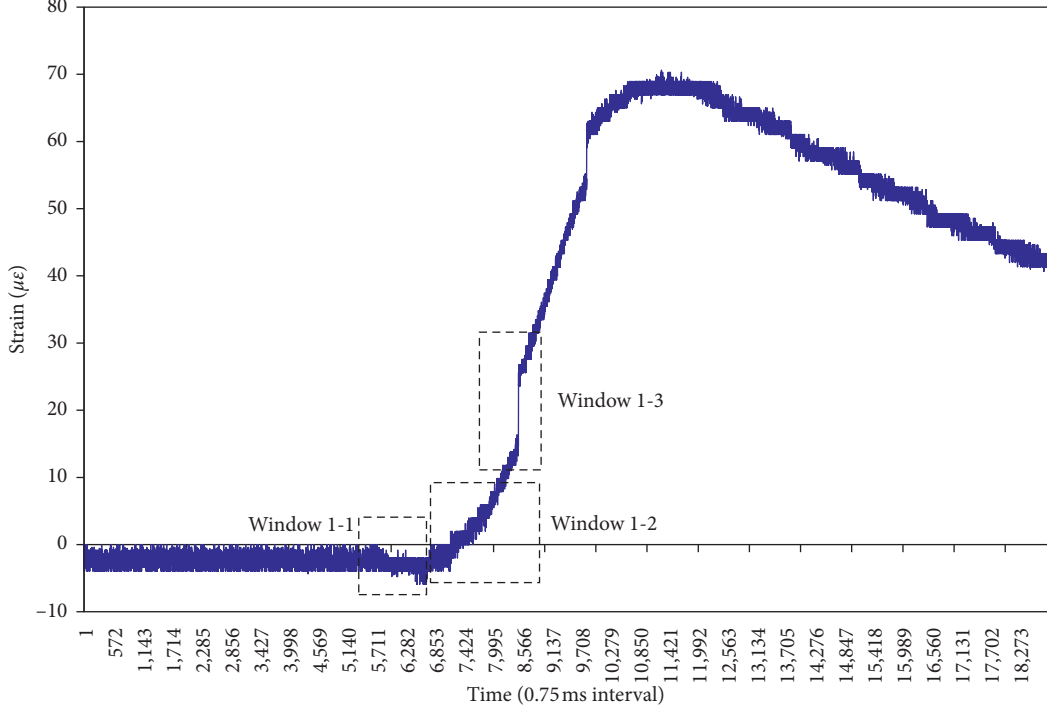


FIGURE 11: First test full-term data.

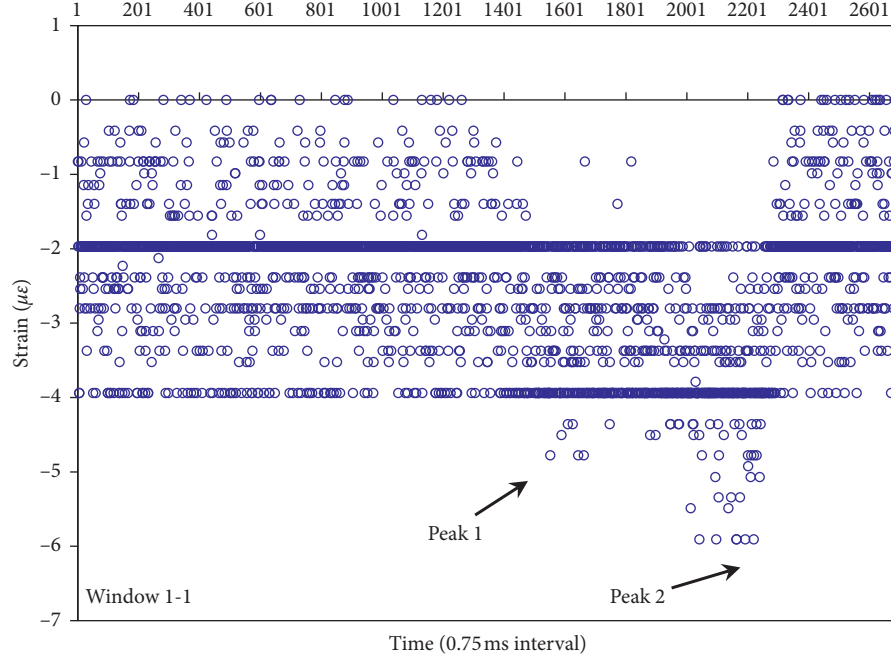


FIGURE 12: Overpressure phase of the first test.

vented overpressure, the second peak in the FBG strain appears, as shown in Figure 12, indicated by the peak 2 arrow.

The compressive strain indicated by peak 2 is greater than that indicated by peak 1. This result shows that after the explosion vent is opened, the vented overpressure is greater than the initial overpressure, which indicates an unbalanced

vent [34]. The compressive strain amplitude is approximately $4 \mu\epsilon$.

With the explosion vent fully opened and the overpressure unloading, the combustion front is transferred to the outside through the explosion vent. The strain of the FBG changes from compressive strain to tensile strain.

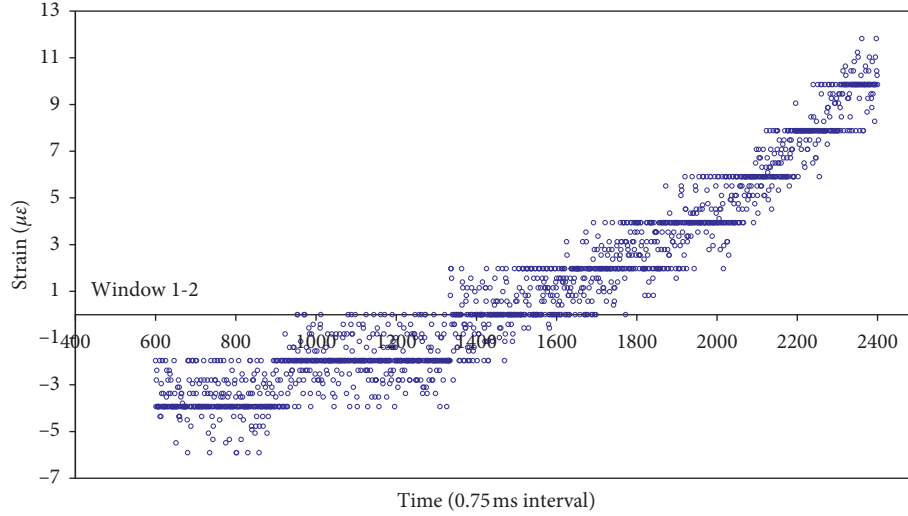


FIGURE 13: Vibration and temperature increase phase of the first test.

Window 1-2 in Figure 11 presents the strain change of the FBG sensor after the overpressure, and Figure 13 shows the enlarged results. The strain increases in a step-like manner, as shown in Figure 13. According to the working condition, the strain change is the result of the combined effects of vibration and temperature after impact. The length of the step gradually decreases, which also proves that the combustion front is gradually approaching the position where the FBG sensor is located, approximately 1.7 m from the ignition position.

Window 1-3 in Figure 11 presents the strain change of the FBG sensor after window 1-2. The strain has a step change, as shown in Figure 14(a). According to the working conditions, the step change in the FBG at this point is generated because the flame front passes through the FBG's position and causes a rapid temperature increase that makes the device undergo a large expansion. In addition to window 1-3, there is another distinct strain step change in the first test, as shown in Figure 14(b). The strain (as shown in Figure 14(a)) caused by the first deflagration flame front is greater than the strain (as shown in Figure 14(b)) caused by the second deflagration flame front formed after the explosion vent is opened. The strain amplitude formed by the flame front passing through the FBG sensor in the first test is shown in Table 1.

As the combustion ends, the temperature begins to decrease and the steel sheet gradually enters the cold-shrinking phase, so the strain gradually decreases, as shown in the full-term data in Figure 11.

There is no visible flame in the opening process of the explosion vent according to the high-speed photography system, as shown in Figure 15.

4.2. Second Test. In the second test, the volume ratio of ethylene is approximately 6.5%, and the explosion vent is pasted and closed with tape. The strain change trend of the grating in the second test is very similar to the result of the first test, but the specific changes are different because of the

different sealing conditions of the explosion vent. The total strain change is shown in Figure 16. The black box in Figure 16 is selected to be enlarged, as shown in Figure 17. The strain change of the FBG is also divided into window 2-1, window 2-2, and window 2-3 for analysis, as shown in Figure 17.

Window 2-1 in Figure 17 is separately plotted, as shown in Figure 18. The strain reflects the overpressure action stage. According to the strain data, the FBG sensor collects the two overpressure peaks in the second test, the positions indicated by peak 1 and peak 2 in Figure 18. The compressive strain indicated by peak 2 in Figure 18 is larger than that indicated by peak 1. This result is the same as that in the first test. According to the working conditions, the volume ratio of ethylene is approximately 6.5% higher than that in the first test, the explosion vent is opened relatively quickly (according to the high-speed photography), and the compressive strain amplitude is approximately $10 \mu\epsilon$.

Window 2-2 in Figure 17 presents the vibration and temperature increase phase after the secondary overpressure, separately plotted as shown in Figure 19. The FBG sensor's strain change reflects the comprehensive change under the influence of structural vibration and temperature. The stepped increase is not as obvious as that in the first test. According to the test condition analysis, the explosion vent is opened at a faster speed than that in the first test (according to the number of photographs taken by high-speed photography), the transfer time for the temperature in the steel plate is short, the combustible gas is vented, the flame front is accelerated, and the heating time is short.

Window 2-3 in Figure 17 shows a step change in the strain caused by the flame front passing through the position of the grating. There are three step changes in the second test, as shown in Figures 20(a)–20(c), and the strain amplitude is shown in Table 2. The second step change is the largest and occurs after the secondary overpressure strain. The third step change is relatively smaller because the combustion products continue to prolong the combustion

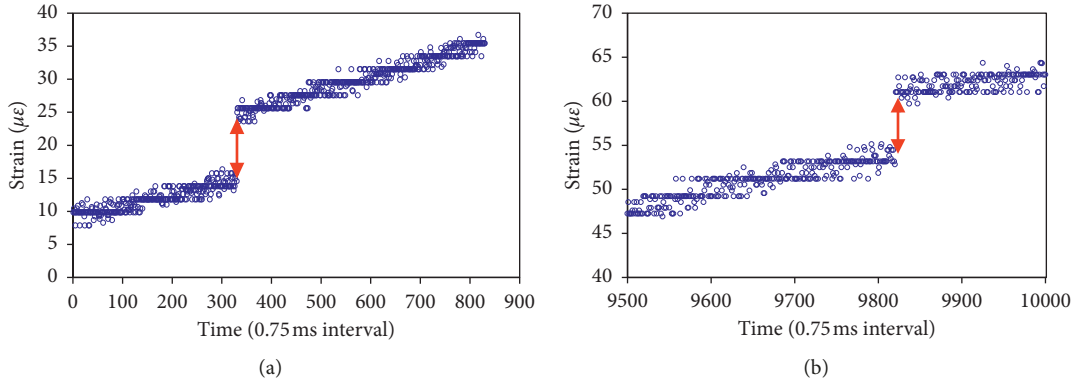


FIGURE 14: The flame front passing phase of the first test. (a) First step change. (b) Second step change.

TABLE 1: Strain amplitude formed by the flame front passing through the FBG sensor in the first test.

First step change ($\mu\epsilon$) (Figure 14(a))	Second step change ($\mu\epsilon$) (Figure 14(b))
10.534	8.21



FIGURE 15: No visible flame in the opening process of the explosion vent in the first test.

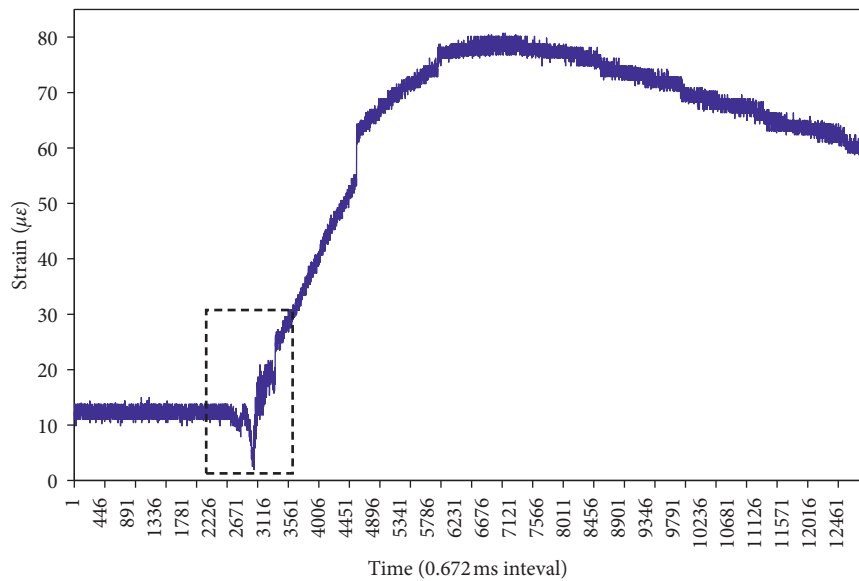


FIGURE 16: Second test full-term data.

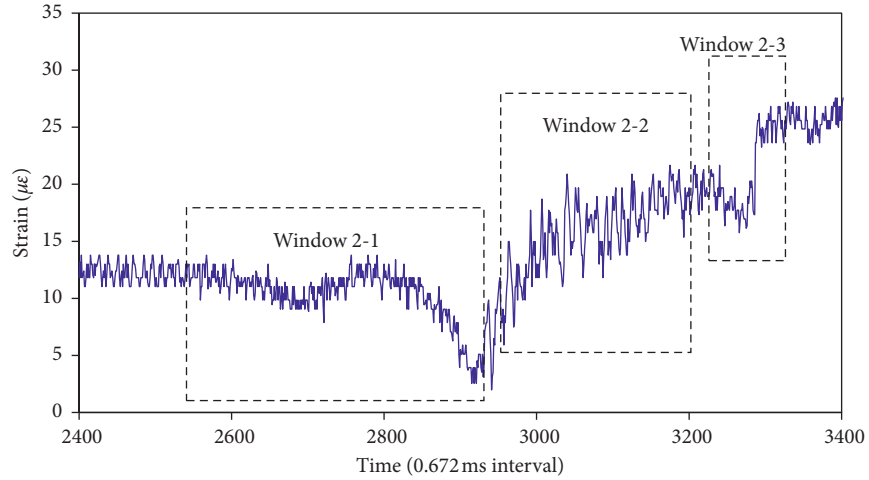


FIGURE 17: Partial enlarged view.

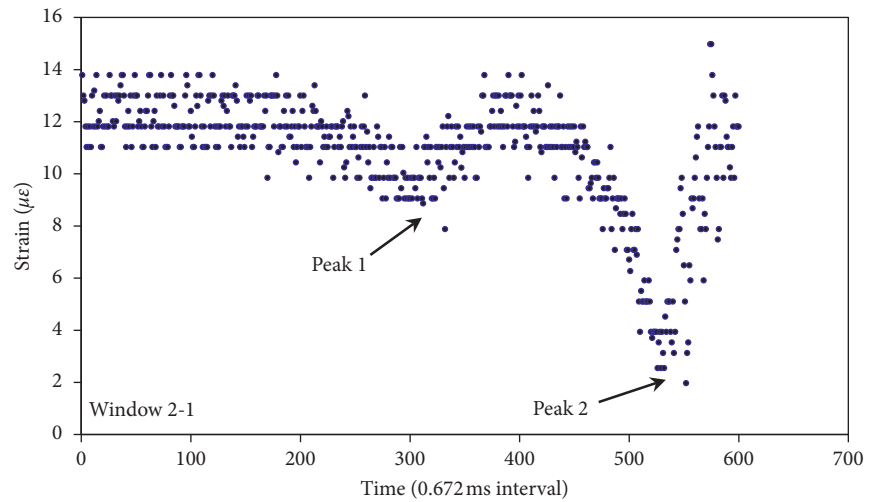


FIGURE 18: Overpressure phase.

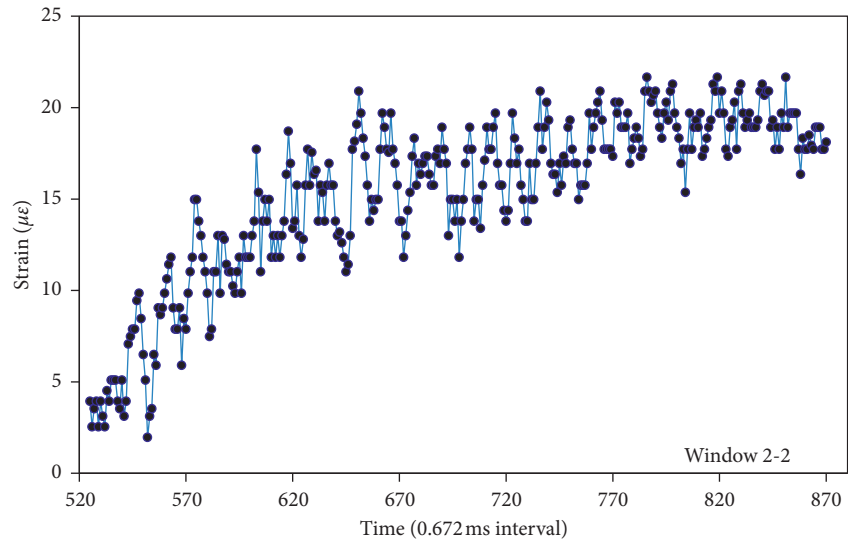


FIGURE 19: Vibration and temperature increase phase.

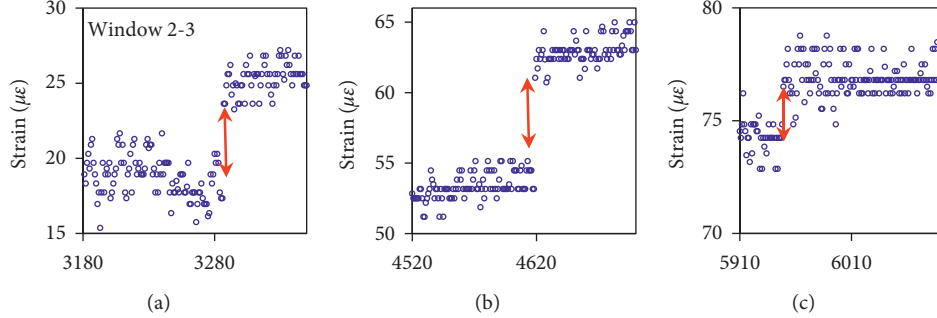


FIGURE 20: Flame front phase. (a) First step change. (b) Second step change. (c) Third step change.

TABLE 2: Strain amplitude formed by the flame front passing through the FBG sensor in the second test.

First step change ($\mu\epsilon$) (Figure 20(a))	Second step change ($\mu\epsilon$) (Figure 20(b))	Third step change ($\mu\epsilon$) (Figure 20(c))
6.294	7.878	1.673

and transfer to the interior of the device after the second deflagration.

According to the high-speed photography, the second test forms a strong and distinct flame after the explosion vent is opened, as shown in Figure 21.

4.3. Third Test. The trend of the overall curve of the strain change in the third test is shown in Figure 22. Two windows, window 3-1 and window 3-2, are selected for analysis.

After window 3-1, which is enlarged as shown in Figure 23, the FBG sensor's strain is different from that in the previous two tests. There is no downward curve due to the compression of the steel plate. Combined with the test conditions, the sealing effect of the explosion vent in the third test is relatively worse than that in the previous two tests. Therefore, after the deflagration occurs, a low initial overpressure will make the cover of the explosion vent open, and the flammable gas is vented quickly and mixes with the air, forming a secondary deflagration. This secondary deflagration occurs near the explosion vent, and the compressive strain acting on the FBG sensor's position by the secondary overpressure is not obvious because the pressure is discharged through the explosion vent; however, the vibration formed at the vent is obvious. The compressive strain amplitude is approximately $2 \mu\epsilon$.

The initial deflagration flame front passing through the FBG sensor forms a step change in the strain, which is shown by the red arrow in Figure 23. The secondary deflagration flame front also passes through the FBG and forms a step change in the strain, as shown by window 3-2 in Figure 22. The strain amplitude formed by the flame front passing through the FBG sensor in the third test is shown in Table 3.

High-speed photography captured a strong flame group at the explosion vent, as shown in Figure 24.

4.4. Fourth Test. The strain change measured by the FBG is shown in Figure 25. The selected part of this figure indicated by the rectangular box is enlarged, as shown in Figure 26.

The FBG sensor's strain includes three phases: the window 4-1 overpressure phase, the window 4-2 vibration and temperature increase phase, and the window 4-3 flame front action phase.

As shown by window 4-1 in Figure 26, the compressive strain formed by overpressure reaches an amplitude of $50 \mu\epsilon$, which is much larger than that in the first three tests. There are two reasons for this finding: First, according to the working condition, under the cumulative action of the first three deflagration tests, the temperature effect inside the device is obvious due to the short test interval, and the initial strain value of the FBG sensor increases from approximately $-2 \mu\epsilon$ in the first test to approximately $17 \mu\epsilon$ in the fourth test. Additionally, the elastic modulus of the steel plate gradually decreases with increasing temperature. As a result, the strain gradually increases under the same overpressure. Second, the ethylene concentration ratio of the fourth test is approximately 7%, which is higher than that in the first three tests.

Window 4-2 in Figure 26 presents the vibration and temperature increase phase after the secondary overpressure. The FBG sensor's strain change reflects the comprehensive change under the influence of structural vibration and temperature.

The high-speed camera records a strong flame group photograph at the explosion vent, as shown in Figure 27. The brightness and deflagration sound of the flame are higher than those of the previous three tests, and the strain step change of the grating caused by the flame front presented by window 4-3 is approximately $15 \mu\epsilon$, which is greater than the amplitude in the first three tests ($8 \mu\epsilon$, $7 \mu\epsilon$, and $11 \mu\epsilon$). The three strain step changes are shown in Table 4.

5. Conclusion

In the four tests, the FBG sensor shows good reusability and is stable and reliable for acquiring data (shown in Figure 28 and Table 5), and this data can reflect important physical processes, such as the overpressure and flame front of the



FIGURE 21: Second test explosion vent flame group.

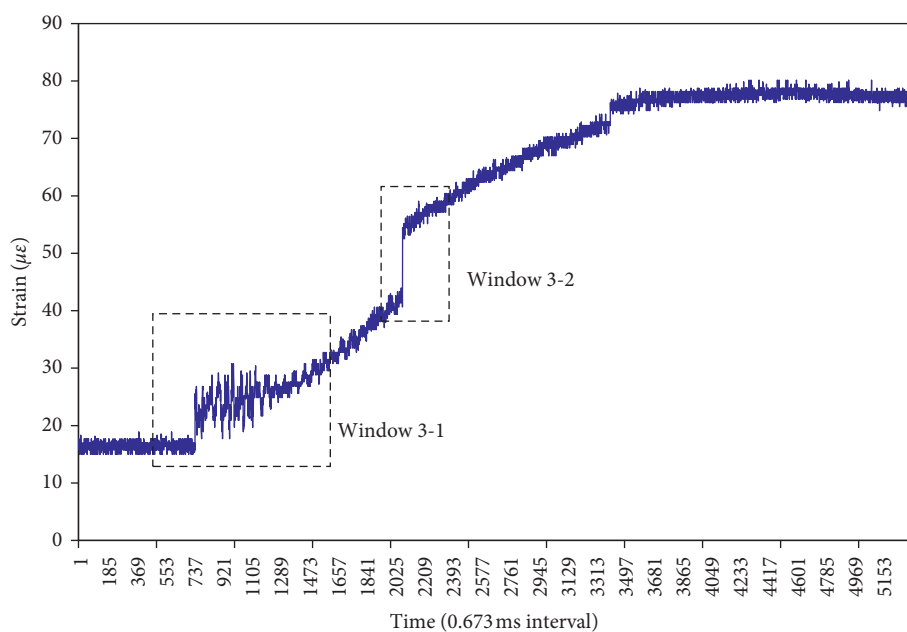


FIGURE 22: Third test full-term data.

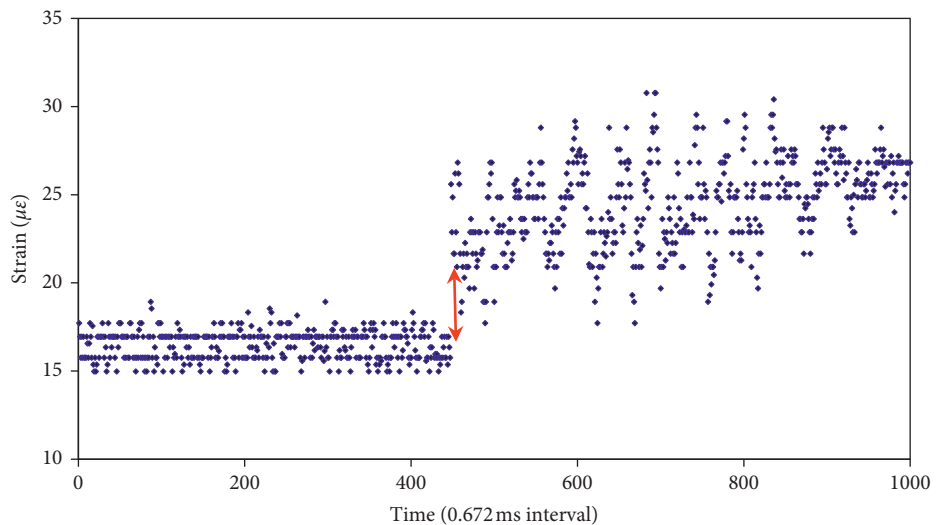


FIGURE 23: Window 3-1.

TABLE 3: Strain amplitude formed by the flame front passing through the FBG sensor in the third test.

First step change ($\mu\epsilon$)	Second step change ($\mu\epsilon$)	Third step change ($\mu\epsilon$)
9.846	13.827	3.951



FIGURE 24: Flame group formed near the explosion vent in the third test.

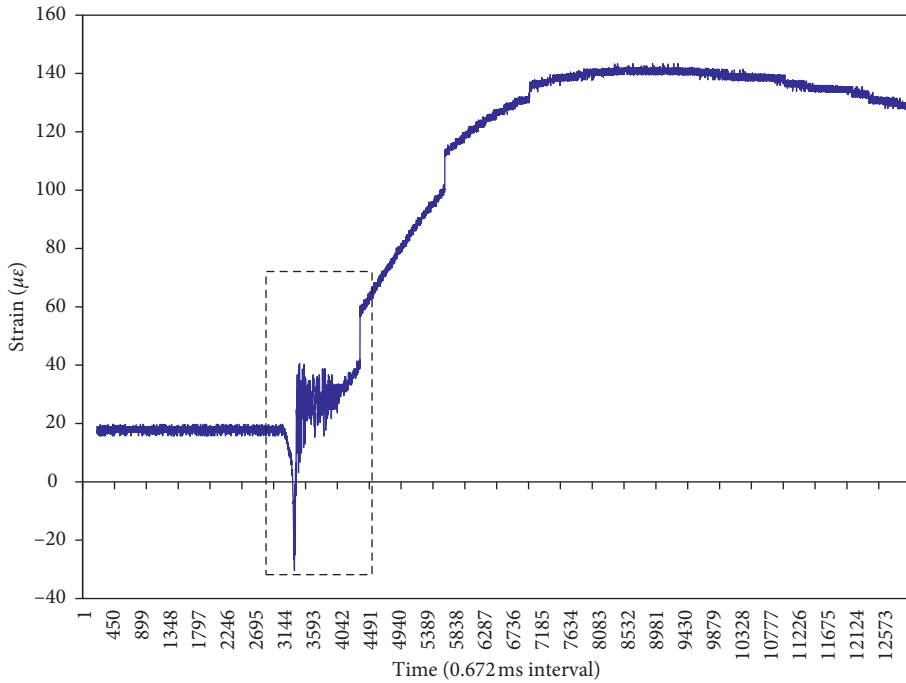


FIGURE 25: Fourth test full-term data.

combustible implosion process. The FBG sensor is simple to package and paste and is worthy of further study for its application in combustible gas implosion tests. However, some problems in the test process need to be further resolved.

- (1) The time when the FBG sensor acquires data is not related to the pressure sensor, so the ignition time cannot be accurately judged. The recording is started before the test and is manually stopped after the test.

- (2) The FBG collects data for the whole test process. The data volume is large, and the information is comprehensive. These data not only reflect the change in the overpressure but also reflect the changes in the flame front and temperature, and further study is needed to distinguish the strain generated by the overpressure from the influence of temperature.
- (3) In this test, only one FBG sensor was installed, and there was no serial arrangement; thus, this test did

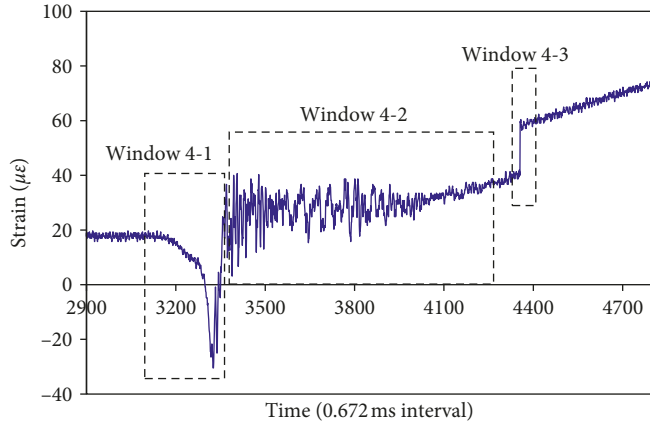


FIGURE 26: Partial enlarged view.

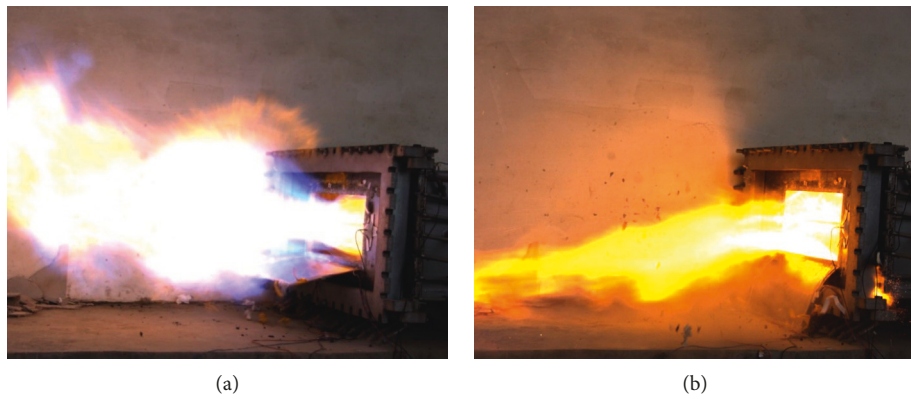


FIGURE 27: Explosion vent flame group in the fourth test.

TABLE 4: Strain amplitude formed by the flame front in the fourth test.

First step change ($\mu\epsilon$)	Second step change ($\mu\epsilon$)	Third step change ($\mu\epsilon$)
19.724	11.854	2.186

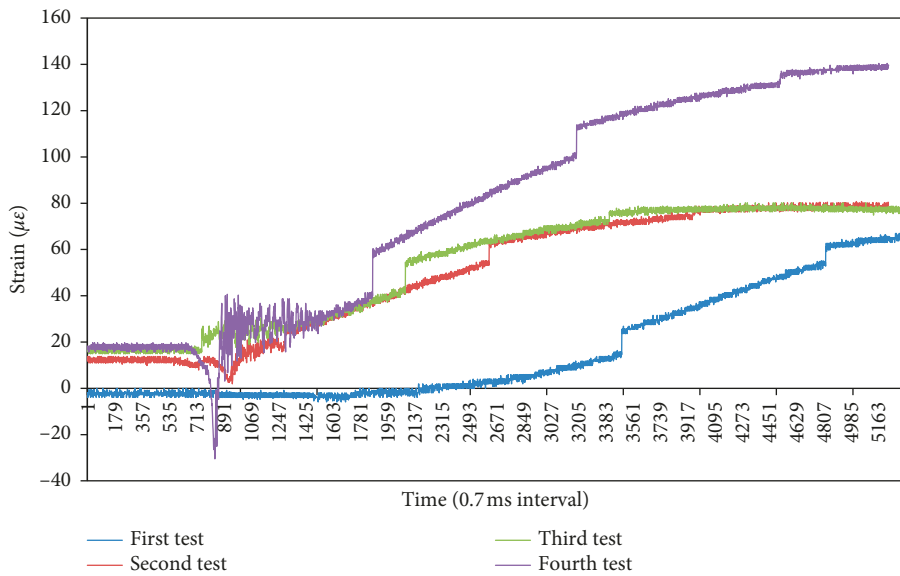


FIGURE 28: The strain data of the four tests.

TABLE 5: Comparison of the overpressure strain results of the four tests.

Number	Initial strain of grating (average of the first 100 data) ($\mu\epsilon$)	Minimum compressive strain ($\mu\epsilon$)	Time from the vent opening to the full extent (ms)
First test	-2.212	-5.907	600
Second test	12.226	1.969	161
Third test	16.425	14.976	140
Fourth test	17.728	-30.453	109

not reflect the quasidistributed monitoring advantage of FBGs.

- (4) The strain measured by the FBG is the strain on the inner surface of the device. To relate this strain to other parameters such as pressure, it is necessary to further establish a mechanical model, obtain an analytical solution, and compare the results with the actual value measured by the pressure sensor to verify the accuracy of the FBG for measurement of strain.

Data Availability

The strain data and photographs used to support the findings of this study are available from the corresponding author upon request.

Conflicts of Interest

The authors declare no conflicts of interest.

Acknowledgments

This work was carried under funding from the National Natural Science Foundation of China (grant no. 41604024).

References

- [1] Z. Wang, "The research development on industrial gas explosion in confined space," *Industrial Safety & Dust Control*, vol. 31, no. 3, pp. 43–46, 2005.
- [2] L. Weidong and Y. Bin, "Study on mechanism of gas explosion induced by coal mine internal fire," in *Proceedings of the 19th EGU General Assembly Conference*, Vienna, Austria, April 2017.
- [3] Q. Bao, Q. Fang, Y. Zhang, L. Chen, S. Yang, and Z. Li, "Effects of gas concentration and venting pressure on overpressure transients during vented explosion of methane-air mixtures," *Fuel*, vol. 175, pp. 40–48, 2016.
- [4] M. Pitzer, G. Kastirke, M. Kunitski et al., "Cover picture: absolute configuration from different multifragmentation pathways in light-induced coulomb explosion imaging (ChemPhysChem 16/2016)," *ChemPhysChem*, vol. 17, no. 16, p. 2448, 2016.
- [5] G.-L. Shen, "New development of strain gauge measurement technique and applications in reactor structures etc. Engineerings," *Atomic Energy Science and Technology*, vol. 42, no. 2, pp. 681–684, 2008.
- [6] G.-L. Shen, "Application of strain electrical measurement and sensing technology in various engineering and domains," *Sensor World*, vol. 1996, no. 9, pp. 681–684, 1996.
- [7] Q. H. Lu, Z. Zhou, D. Li, and T. N. Guo, "Structural strain modes identification method by eigensystem realization algorithm," *Journal of Mechanical Strength*, vol. 26, no. 1, pp. 1–5, 2004.
- [8] M. A. Davis, A. D. Kersey, J. Sirkis, and E. J. Friebel, "Shape and vibration mode sensing using a fiber optic Bragg grating array," *Smart Materials and Structures*, vol. 5, no. 6, pp. 759–765, 1996.
- [9] B. J. Arritt, C. Klimcak, E. Pollard, H.-P. Dumm, and T. Murphey, "Shape determination of large deployable space structures through the use of fiber-optics with integrated fiber-Bragg's gratings," in *Proceedings of the Sensor Systems and Networks: Phenomena, Technology, and Applications for NDE and Health Monitoring 2007*, vol. 6530, San Diego, CA, USA, April 2007.
- [10] Q. Ya, L. Shen, W. Hu, Y. Zhang, and L. Feng, "Shape re-building and positioning method of search and rescue robot endoscope in ruin crack," *Chinese Journal of Scientific Instrument*, vol. 36, no. 12, pp. 2782–2789, 2015.
- [11] E. Wolfgang, "Optical fiber grating strain sensor network for X-38 spacecraft health monitoring," in *Proceedings of the Fourteenth International Conference on Optical Fiber Sensors*, vol. 4185, pp. 888–891, Venice, Italy, November 2000.
- [12] A. Derkevorkian, S. F. Masri, J. Alvarenga, H. Boussalis, J. Bakalyar, and W. L. Richards, "Strain-based deformation shape-estimation algorithm for control and monitoring applications," *AIAA journal*, vol. 51, no. 9, pp. 2231–2240, 2013.
- [13] R. Di Sante, "Fibre optic sensors for structural health monitoring of aircraft composite structures: recent advances and applications," *Sensors*, vol. 15, no. 8, pp. 18666–18713, 2015.
- [14] J. Ou, Z. Zhou, Z. Wu et al., "Intelligent monitoring of heilongjiang hulan river bridge based on fbg," *China Civil Engineering Journal*, vol. 37, no. 1, pp. 45–49, 2004.
- [15] T. H. T. Chan, L. Yu, H. Y. Tam et al., "Fiber Bragg grating sensors for structural health monitoring of Tsing Ma Bridge: background and experimental observation," *Engineering Structures*, vol. 28, no. 5, pp. 648–659, 2006.
- [16] H. Zhu, J. Yin, W. Jin, and D. Gu, "Health monitoring of foundations using fiber Bragg grating sensing technology," *China Civil Engineering Journal*, vol. 43, no. 6, pp. 109–115, 2010.
- [17] L. Sun, *Analysis of Application Problems of Fiber Bragg Grating Sensors*, Science Press, Beijing, China, 2012.
- [18] Q. Zhang, Y. Wang, Y. Sun, L. Gao, and Y. Yue, "Hilbert-Huang transform based method for monitoring the crack of concrete arch by using FBG sensors," *Optik*, vol. 127, no. 6, pp. 3417–3422, 2016.
- [19] Q. Zhang, Y. Wang, Y. Sun et al., "Using custom fiber Bragg grating-based sensors to monitor artificial landslides," *Sensors*, vol. 16, no. 9, pp. 1417–1430, 2016.
- [20] H. Gong, Y. Xiao, Y. Tu, H. Song, and X. Dong, "Vibration detection characteristics of FBG sensor and resistance strain gauge," *Infrared and Laser Engineering*, vol. 42, no. 3, pp. 811–813, 2013.
- [21] X. Zhang, S. Xie, H. Niu, P. Zhang, and B. Jia, "Research on dynamic measurement technology of fiber optic sensors and their development," *Journal of Vibration, Measurement & Diagnosis*, vol. 35, no. 3, pp. 409–416, 2015.

- [22] X.-D. Wu, C. Schmidt-Hattenberger, K. Krüger, and J. Chen, "Temperature-controlled fiber Bragg grating dynamic strain detection system," *Sensors and Actuators A: Physical*, vol. 119, no. 1, pp. 68–74, 2005.
- [23] A. Cusano, A. Cutolo, J. Nasser, M. Giordano, and A. Calabro, "Dynamic strain measurements by fiber Bragg grating sensor," *Sensors & Actuators a Physical*, vol. 110, no. 1–3, pp. 276–281, 2004.
- [24] P.-Y. Zhu, Y.-C. Lin, and W. Wang, "Fiber Bragg grating sensor for high frequency strain measurement," *Opto-Electronic Engineering*, vol. 34, no. 6, pp. 135–139, 2007.
- [25] G. Rodriguez, R. L. Sandberg, B. M. Lalone et al., "High pressure sensing and dynamics using high speed fiber Bragg grating interrogation systems," *Applied Physics Letters*, vol. 109, no. 16, 2016.
- [26] D. M. Karabacak, S. K. Ibrahim, Y. Koumans, B. Meulblok, and R. Knoppers, "High-speed system for FBG-based measurements of vibration and sound," in *Proceedings of the Fiber Optic Sensors and Applications XIII*, vol. 9852, Baltimore, MD, USA, May 2016.
- [27] Y. Sun, J. Liu, Y. Wang et al., "Principles and application of polyimide fiber Bragg gratings for surface strain measurement," *Applied Sciences*, vol. 7, no. 10, p. 995, 2017.
- [28] G. Rodriguez and S. Gilbertson, "Ultrafast fiber Bragg grating interrogation for sensing in detonation and shock wave experiments," *Sensors*, vol. 17, no. 2, p. 248, 2017.
- [29] W. Guo, J. Cui, and J. Jang, "Dynamic response analysis of plate under combustion and explosion," *Engineering Mechanics*, vol. 16, pp. 505–509, 1999.
- [30] L. Sun, H. Li, T. Zhu, L. Ren, and R. Dong, "Dynamic characteristic and application range of FBG strain sensor," *Journal for Vibration And Shock*, vol. 25, no. 3, pp. 29–34, 2006.
- [31] Y. Sun, Y. Wang, Z. Zhang et al., "Analysis and experimental research on the principle of surface bonded FBG strain transfer," *Journal of Functional Materials*, vol. 47, no. 7, pp. 07046–07050, 2016.
- [32] Z. Zhang, Y. Wang, Y. Sun, and Q. Zhang, "Influence of adhesive on surface-bonded FBG sensor strain transfer coefficient," *Acta Materiae Compositae Sinica*, vol. 33, no. 11, pp. 2537–2542, 2016.
- [33] Y. Wang, Z. Zhang, Y. Sun, and Q. Zhang, "The influence of different surface paste on FBG strain transfer," *Piezoelectrics & Acoustooptics*, vol. 38, no. 1, pp. 106–110, 2016.
- [34] D. Bradley and M. Alam, "The venting of gaseous explosion in spherical vessels.I-theory and experiment," *Combustion and Flame*, vol. 32, pp. 221–236, 1978.

